Catalysis Today 429 (2024) 114507

Contents lists available at ScienceDirect

Catalysis Today

journal homepage: www.elsevier.com/locate/cattod

Cost effective synthesis of 3-dimensional V_4O_9: A promising high-capacity lithium cathode

Chandrasekar M Subramaniyam [a,*], Alois Kuhn [a], Ester García González [b], Olga Guerrero-Pérez [c], Enrique Rodríguez-Castellón [d], Flaviano García-Alvarado [a,*]

[a] Department of Chemistry and Biochemistry, Facultad de Farmacia, Universidad San Pablo-CEU, CEU Universities, Boadilla del Monte, 28668 Madrid, Spain
[b] Departamento de Química Inorgánica, Facultad de Ciencias Químicas, Universidad Complutense de Madrid, Madrid 28040, Spain
[c] Departamento de Ingeniería Química, Facultad de Ciencias, Universidad de Málaga, 29071 Málaga, Spain
[d] Departamento de Química Inorgánica, Facultad de Ciencias, Universidad de Málaga, 29071 Málaga, Spain

ARTICLE INFO

Keywords:
V_4O_9 Nanoparticles
Solvothermal synthesis
Lithium-ion battery
Cathode

ABSTRACT

The earthly abundant vanadium exhibits multi-oxidation states and different crystalline structures in their oxide compounds offering unique electrical, opto-electronic, and catalytic properties to be applicable for various applications including energy storage materials. The stable vanadium oxides (V_2O_5, VO_2, V_2O_3) are mostly studied while metastable oxides such as V_4O_9 is less explored. The latter possesses a tridimensional (3D)-tunnel defect type structure with different polyhedral wherein VO_5 pyramids and VO_6 octahedra are connected by corner oxygen atoms from the VO_4 tetrahedra with V^{4+} and V^{5+} oxidation states, respectively, making it an appealing host candidate for lithium-ions insertion. Herein, we present a cost-effective single pot synthesis of 3D V_4O_9 nanoparticles using versatile low temperature solvothermal method. The obtained material has been fully characterised in terms of phase identity and crystal structure using x-ray diffraction, Raman spectroscopy and high-resolution-transmission-electron-microscopy while surface composition and valence- and/ oxidation states using x-ray photoelectron spectroscopy followed by investigation of its electrochemical performance against lithium. Upon first discharge, V_4O_9 could intercalate ~6 Li^+ per formula unit corresponding to highest discharge capacity of 464.5 mA h g^{-1} and a reversible first Coulombic efficiency of 75.3% between 1.5 – 4.0 V against Li in a half-cell configuration. In the long run, the V_4O_9 exhibited a reversible capacity of 160.8 mA h g^{-1} at 100 mA g^{-1} even after 2000 cycles against lithium rendering it as suitable positive electrode with high capacity and cyclability for lithium-ion battery applications.

1. Introduction

To nullify the greenhouse gases emissions without hampering growing energy demand renewable energy resources like sun, tidal, wind etc. are steadily gaining importance in the energy mix of the future [1]. However, these intermittent natural sources require high energy density storage devices such as batteries and supercapacitors to store electrical energy into chemical energy and deliver electricity when required/discharged. The batteries possess high energy density and low power density and vice-versa for the supercapacitors [2]. Lithium-ion battery (LIB) technology commercialized in 1990s by Sony Inc. have revolutionized the world of electronics with superior energy densities, extensive cycle life, low self-discharge and environmental benignity and are now being explored to electrify plug-in electric vehicles (EVs) [3].

Development of insertion cathode host electrode materials determines the cycle life, safety, and overall energy density of the LIBs. Till date, various cathode host electrode materials such as transition-metal-oxides [4,5], olivine type [6], polyanion-type [7,8] and Prussian blue analogues (PBAs) [9] are explored for LIBs. But these state-of-art cathodes are limited due to low gravimetric capacity, limited long-term cyclability and critical raw materials (Li and Co) hampering their large-scale deployment use in building EVs [10].

Vanadium oxides with different polymorphs (such as V_2O_5, $V_2O_5{\cdot}nH_2O$, VO_2, V_2O_3, $V_3O_7{\cdot}H_2O$, V_6O_{13}) are explicitly studied as promising cathodes due to the vast vanadium resources in the earth's crust and their unique open framework structures for ultrafast 2D interlayer diffusion with extraordinary electrochemical property due to their diverse oxidation redox couples (V^{2+} to V^{5+}) [11–16]. The stable

* Corresponding authors.
E-mail addresses: mayandi@ceu.es (C. M Subramaniyam), flaga@ceu.es (F. García-Alvarado).

https://doi.org/10.1016/j.cattod.2024.114507
Received 22 November 2023; Accepted 1 January 2024
Available online 4 January 2024

vanadium oxides (V_2O_5, VO_2, V_2O_3) are mostly studied while metastable mixed valence oxides such as V_4O_9 is less explored [17]. The latter possesses orthorhombic structure with different polyhedra wherein VO_5 pyramids and VO_6 octahedra are connected by corner oxygen atoms from the VO_4 tetrahedra with V^{+4} and V^{5+} oxidation states, respectively making it an appealing host candidate for Li^+ ions [18,19].

Typically, V_4O_9 is synthesized by the reduction of V_2O_5 using reducing agents (SO_2 and Sulfur) between 300 – 500 °C but often resulted in over-reduced final products containing other vanadium oxides (V_6O_{13} and VO_2) [18,20]. Therefore, solvothermal process is a facile single-step method to reduce V_2O_5 to V_4O_9 by using various reducing solvents such as tetraethylene glycol and tetrahydrofuran [21–23]. Qiaoran *et al.,* reported solvothermal prepared V_4O_9 as zinc-ion battery host cathode exhibiting fast reversible insertion of Zn-ions and electron transport due to its unique tunnel structure and mixed-valence (V^{5+}/V^{4+}) induced metallic behaviour [23]. Pang *et al.*, synthesized 3D V_4O_9 microflower structures exhibiting good supercapacitor performance with a specific capacitance of 392 F g^{-1} at 0.5 A g^{-1} retaining 75% capacitance after 2000 cycles [21]. Hammouche [24] reported V_4O_9 as type I intercalation compound exhibiting 4 Li^+ per formula at low current density and recently, Premkumar *et al.,* reported synthesis of pure micron-sized V_4O_9 phase using mild reducing gas stream (NH_3/Ar) at 300 °C as potential lithium cathode exhibiting 225 mA h g^{-1} for 50 cycles between 3.5 - 1.8 V against lithium [19].

Herein, we present one-pot synthesis of 3-dimensional V_4O_9 nanoparticles using cost-effective versatile solvothermal method to reduce V_2O_5 using non-viscous low boiling point acetonitrile as solvent without any post-annealing process and test its performances as Li-ion host cathode.

2. Experimental methods

2.1. Synthesis of V_4O_9 nanoparticles

All chemicals were purchased from Sigma Aldrich and were used without any purification. The commercial pristine V_2O_5 powders were dry ball milled with ball to powder weight ratio of 20:1 at 300 rpm for 150 mins (Fritsch's Planetary Micro Mill; Model: Pulverisette 7). The collected ball milled V_2O_5 was marked as BMVO. To prepare V_4O_9 nanoparticles: BMVO was dispersed in acetonitrile (6:1 wt. to volume ratio) using magnetic stirring at 300–400 rpm for 30–40 mins. The dispersion was decanted to 125 mL Teflon-liner and then sealed in a stainless-steel hydrothermal autoclave reactor. The set-up was heated in an oven at 230 °C for 8 h. After cooling to room temperature, the black sediments were collected and washed several times with ethanol prior to drying at 60 °C overnight. The powders were then ground and labelled as V_4O_9.

2.2. Material characterizations

X-ray diffraction (XRD, Bruker D8) of the powdered samples were measured using Cu K_α radiation ($\lambda = 1.5418$ Å) between $2\theta = 10°$ to 80° and crystal structures were determined from the diffractogram using FullProf refinement software. Spherical harmonics expansion had been implemented in FullProf to better describe nanostructured samples instead of classic shape parameters. The morphology analysis was carried out using field-emission-scanning-electron-microscopy (FESEM, Thermo Fisher Scientific, Model: Prisma E). The sample for transmission electron microscopy (TEM) was ultrasonically dispersed in n-butanol and transferred to a carbon-coated copper grid. Selected area electron diffraction (SAED) and high-resolution transmission electron microscopy (HRTEM) were performed on a JEOL JEM GRAND ARM 300cFEG electron microscope with corrected aberration in the objective lens and working at 300 kV (point resolution of 0.05 nm). X-ray photoelectron spectroscopy (XPS) was conducted using a SPECS Phoibos 100 analyser installed in a high-vacuum chamber with a base pressure of less than 10^{-8} mbar, and X-ray excitation was provided by an Al K_α irradiation source with photon energy $h\nu$ of 1486.6 eV at 12 kV and 120 W power. XPS binding energy spectra were recorded at a pass energy of 23.5 eV in fixed analyser transmission mode in a Versa-Probe II PHI spectrometer, and data analysis was carried out using the Multipak 9.0 software package with all spectra calibrated against C 1*s* = 284.6 eV. Raman spectroscopy was performed with μ-Raman JASCO NRS-5100 spectrometer in the following conditions: 785 nm laser; 1.0 and 2.5 mW (Power); acquisition time of 10 s at 100x objective lens. Low powers were employed to avoid sample damaging. The specific surface area (in $m^2\ g^{-1}$) considered as the best approximation to the intercalation active area, was determined by nitrogen adsorption-desorption (Brunauer-Emmett-Teller (BET) method) experiments (Micromeritics ASAP 2020 analyzer).

2.3. Electrochemical characterizations

V_4O_9 sample was electrochemically tested as positive electrode against lithium in half-cell configuration. The V_4O_9 was blended with super P carbon (conducting agent) and polyvinylidene fluoride (PVDF) binder with respective wt. ratio of 7:2:1, using N-methyl-2-pyrrolidone (NMP) solvent. The blended slurry was tape-cast over carbon-coated aluminum current collector using 20 μm doctor's blade and vacuumed dried at 120 °C overnight. The electrode was disc-cut to 12 mm diameter with active material weighed about ~0.8 - 1.4 mg cm^{-2}. Half-cell coin cells (CR 2032) configuration were assembled inside an argon filled glove box maintained at 0.1 ppm H_2O and 0.1 ppm O_2 level. The V_4O_9 electrode was used as a working electrode while lithium metal discs as counter/reference electrodes separated by Whatman's glassfibre (Grade: G/F) separator impregnated/wetted with Solvionic's LiFSI:PYR14 FSI (2:3 mol ratio) electrolyte for lithium cells. All cells exhibited an open-circuit-voltage (OCV) of ~3.3 – 3.4 V upon resting 24 h. These cells were (discharge-charge) cycled between 1.5 – 4.0 V for lithium cells at constant current density (in mA g^{-1}) unless specified using a Neware Multichannels Battery Tester (Neware CT-4000, China) and Arbin multichannel battery tester (Texas Instruments, USA). The specific capacity was calculated based on the net weight of active material unless specified. The cyclic voltammagram (CV) and electrochemical-impedance-spectroscopy (EIS) were measured using BioLogic VMP3 instruments (BioLogic, France). The impedance of two-electrode cells was measured between 0.1 MHz – 10 mHz frequency range under an AC voltage of 5 mV amplitude and data were analyzed using the Z-Fit programme of EC-lab software ®.

3. Results and discussion

The starting bulk V_2O_5 (99.9% purity, Sigma Aldrich) consisted of large chunks of microparticles (Fig. 1**a**). Upon dry ball-milling at 300 rpm for 150 min, the particles are reduced to nanoparticles (labelled as BMVO, Fig. 1**b**) without any change in the pristine orthorhombic phase (Fig. 1**c**). The ball milled V_2O_5 (BMVO) consists of aggregation of nanoparticles as deduced from the corresponding peak broadening in its XRD pattern (Fig. 1**c**). XPS spectra of BMVO are shown in Fig. 1 d,e. The V $2p_{3/2}$ spectrum indicates the presence of a small amount of V(IV) at 516.3 eV (Fig. 1 d) with corresponding lattice oxygen (O 1*s*) components - V(IV) oxide and V(V) oxide (530.4 eV) and HO-V interactions (531.4 eV) as shown in Fig. 1**e**. These BMVO nanoparticles were used in the V_4O_9 synthesis by versatile solvothermal process using acetonitrile as solvent. The defect induced V(IV) could be possible active sites for selective partial reduction of BMVO to V_4O_9 phase. Besides, it is a well-known catalyst for any partial oxidation (not just that of acetonitrile) with an appropriate V^{5+}/V^{4+} ratio to make this reduction-oxidation (redox) cycle to occur in the reaction [25]. This observation is similar in accordance with Brazdil *et al.,* whose study reported the selective oxidation of acetonitrile using vanadium oxide catalyst [25,26].

The X-ray diffraction pattern of V_4O_9, obtained with this low-

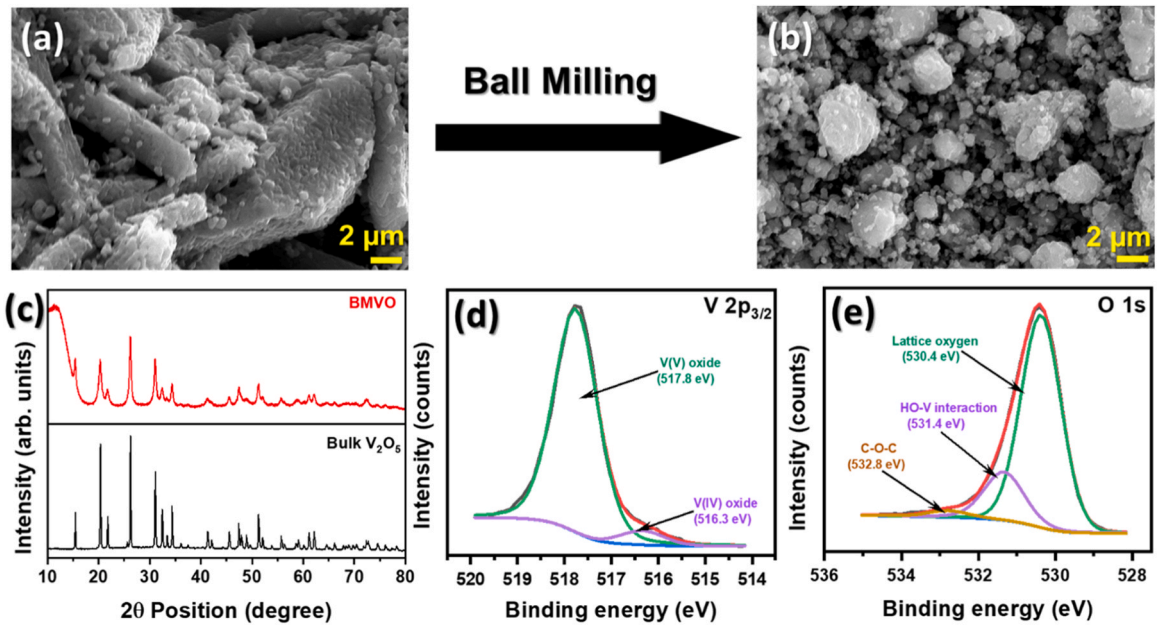

Fig. 1. Morphology of (a) bulk V_2O_5 and (b) ball milled V_2O_5 nanoparticles (BMVO); (c) XRD patterns of bulk V_2O_5 and ball milled V_2O_5 nanoparticles (BMVO); High resolution XPS spectra of BMVO: (d) V $2p_{3/2}$; (e) O 1*s*.

temperature method, has been completely indexed in the orthorhombic system and *Cmcm* space group. Through the structural refinement carried out (Fig. 2**a**), the lattice parameters have been obtained for the orthorhombic unit cell *a = 10.3814(9) Å, b =8.1667(9) Å, c =16.595(2) Å* and with a *unit cell volume =1407.0(3) Å*^{3}. The most important crystallographic parameters of the structural refinement of V_4O_9, such as atomic positions in the form of fractional coordinates, Debye-Waller or isotropic atomic displacement factors and occupancies are collected in Table S1.

According to Fig. 2**b**, the structure of V_4O_9 consists of square-based pyramids $V(1)O_5$ (green) sharing oxygen vertices of the basal plane with four tetrahedra $V(3)O_4$ (blue) in the *ab* plane and the apical oxygen vertex with another square-based pyramid $V(1)O_5$ along the *c* axis. Furthermore, $V(1)O_5$ pyramids (green) share an oxygen edge with $V(2)O_6$ octahedra in the *ab* plane, these $V(2)O_6$ octahedra being connected to each other by a common oxygen vertex along the *c* axis. The connection between the three types of polyhedra $V(1)O_5$, $V(2)O_6$ and $V(3)O_4$ gives rise to an open three-dimensional structure with mixed vanadium oxidation states + 4 and + 5, respectively, in combined octahedron & pyramid and tetrahedron rendering V_4O_9 as a suitable host for lithium ions.

Sample was further analyzed by HRTEM. The synthesized V_4O_9 is constituted by agglomerated flake-shaped nanocrystallites (5–20 nm average size). Fig. 3**a** shows one of these agglomerates. The periodic contrasts observed in the crystallites show some of the interplanar spacings characteristic of the structure. Inset shows the corresponding electron diffraction ring pattern where diffraction rings assigned to characteristic d_{hkl} spacings of the V_4O_9 have been indexed according to the symmetry of the *Cmcm* crystal structure. Crystallites tend to grow in the (001) plane or in close orientations, and in this projection, they can reach sizes above 200 nm (Fig. 3**b**).

The surface composition of V_4O_9 and mixed valence state of vanadium is further probed using surface analytical XPS technique as shown in Fig. 4**a-c**. The high-resolution V $2p_{3/2}$ spectrum obtained by short exposure beam time to avoid oxidation of vanadium as shown in Fig. 4**a**. The V $2p_{3/2}$ could be deconvoluted into two distinct peaks at 516.5 eV and 517.6 eV corresponding to V^{4+} and V^{5+}, respectively [23]. The area under V^{4+} and V^{5+} peaks equal 1:1.87 demonstrating an average 4.65 oxidation state for vanadium ions. The charge compensation is balanced with the lattice oxygen species observed at 530.5 eV of O 1*s* (Fig. 4**b**). The presence of cyano group (-CN) at 399.6 eV and its interaction with vanadium ions (Fig. 4**c**) confirms possible nitrogen doping induced by partial oxidation of acetonitrile [26]. Further, the nature of chemical interactions and bonding of vanadium are further deduced using surface sensitive Raman spectroscopy as shown in Fig. 4**d**. The characteristic bands at 407.02, 751.07 and 900.87 cm^{-1} pertain to vibrations of V_4O_9 [27] while 275.92 cm^{-1} band assigned to the bending vibrations of O═V bonds. The band at 477.7 cm^{-1} associates with the V-O-V bridging

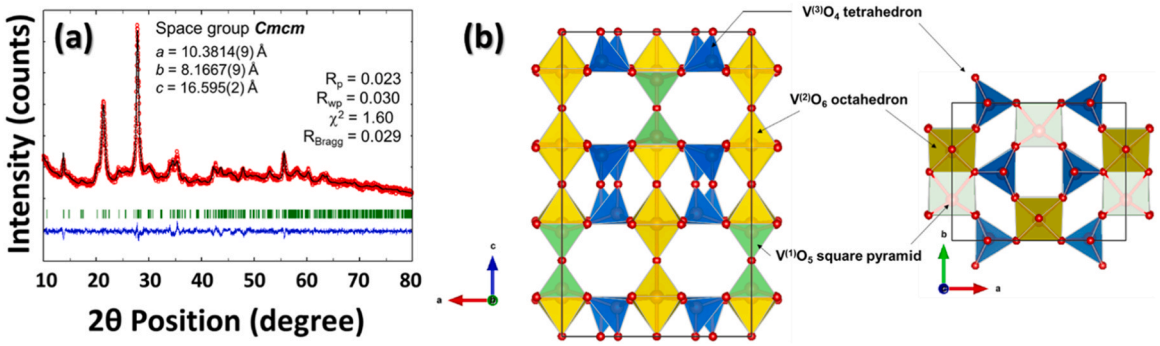

Fig. 2. (a) Rietveld refinement of V_4O_9 nanoparticles; (b) Structure of V_4O_9 projected onto the *ac* plane (left) and *ab* plane (right). The unit cell is shown.

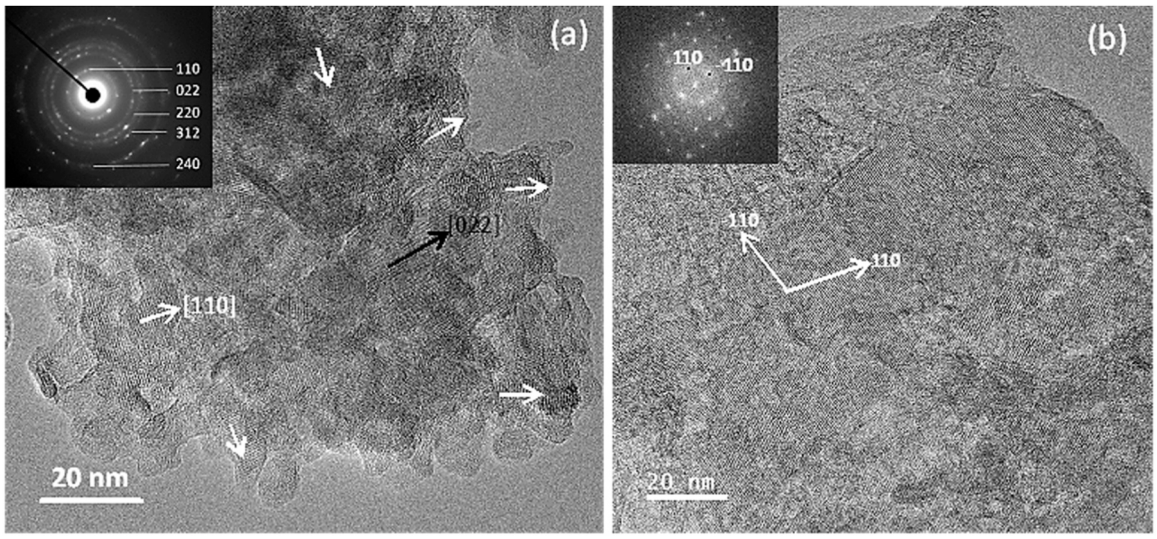

Fig. 3. (a) High resolution micrograph of a nanocrystal agglomerate. Inset shows the corresponding ring electron diffraction pattern indexed on the basis of the *Cmcm* structure symmetry of V_4O_9; (b) Crystallite oriented close to [001]. FFT in the inset illustrates the almost single crystal nature of the particle.

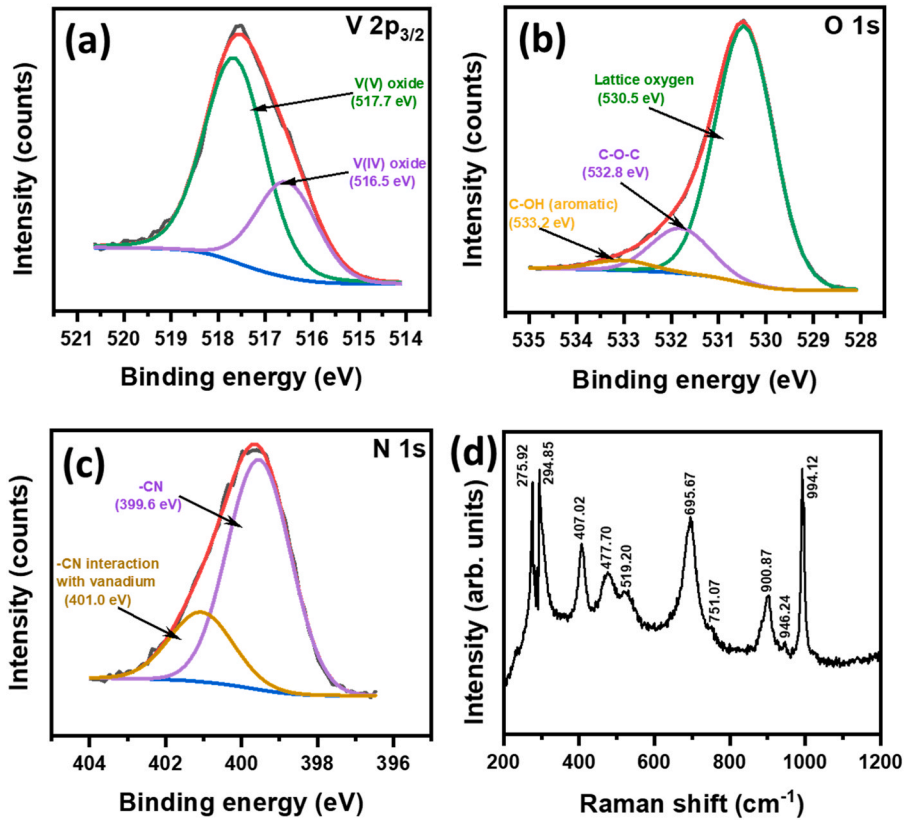

Fig. 4. High resolution XPS spectra of V_4O_9 (a) V $2p_{3/2}$; (b) O 1*s*; (c) N 1*s*; (d) Raman spectrum of V_4O_9.

bond and 294.85 cm^{-1} band is assigned to bending of bonds near co-ordinated oxygen atoms [28]. The 519.2 and 695.67 cm^{-1} bands correspond to two stretching modes (parallel and perpendicular) to the *ab*-plane while the highest wavelength 994.12 cm^{-1} attributes to V═O stretching [28,29].

Fig. 5 depicts the electrochemical performances of V_4O_9 as positive electrode in half-cell coin-cell configuration against lithium between 1.5 – 4.0 V. Firstly, we studied the electrochemical performance of V_4O_9 using Solvionic's organic carbonate based (1 M $LiPF_6$ in 1:1 (v/v) EC: DMC) electrolyte (Fig. S1). At low current density of 10 mA g^{-1}, the V_4O_9 delivered a discharge capacity of 384.9 mA h g^{-1} with 89.6% first Coulombic efficiency which is highest reported for vanadium oxide-based cathode using carbonate electrolyte (Table S2). However, the specific capacity deteriorates with cycle numbers dropping to 47 mA h g^{-1} after 100 cycles (Fig. S1). This is possibly due to the vanadium dissolution in carbonate electrolyte leading to the capacity fade [30]. Upon replacing carbonate electrolyte with Solvionic's LiFSI:PYR14 FSI (2:3 mol ratio) electrolyte, V_4O_9 could intercalate ~6 Li^+ as compared to only 3 Li^+ by BMVO (Fig. 5**a**) corresponding to respective, specific discharge capacity of 464.8 mA h g^{-1} and ~442 mA h g^{-1}. The

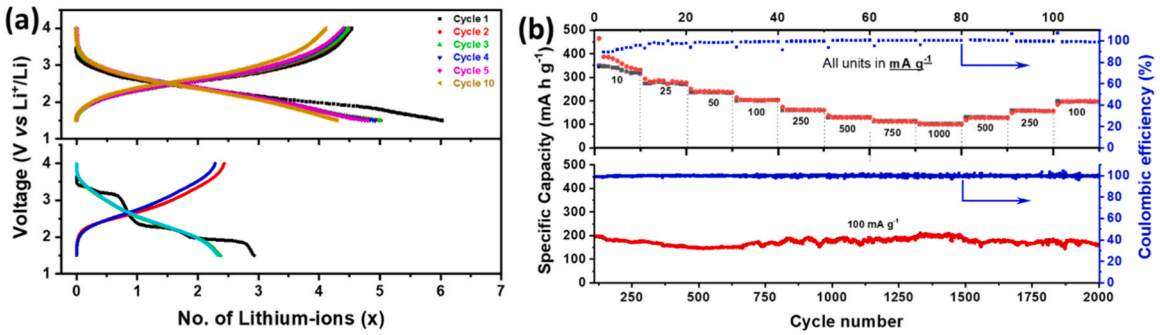

Fig. 5. Electrochemical performance of V_4O_9 against lithium between 1.5 – 4.0 V. (a) charge-discharge plots of V_4O_9 and V_2O_5 nanoparticles; (b) Rate test of at V_4O_9 nanoparticles at different current densities and long cycle stability at 100 mA g^{-1}.

latter discharge-charge curve shows multitude of redox mechanisms as compared to classic `S-type´ curve for V_4O_9 (irrespective of electrolyte) which agrees with literature [19,24]. The first Coulombic efficiency (CE) of V_4O_9 is 75.3% while maintained 99.9% CE in the subsequent cycles. The BMVO could deliver 230 mA h g^{-1} at 10 mA g^{-1} for 70 cycles with constant depreciation of its electrochemical performance with cycle number (Fig. S2). Whereas subjecting V_4O_9 to rate test at various current densities (10 - 1000 mA g^{-1}), it delivered a reversible capacity of 331.4 mA h g^{-1} at 10 mA g^{-1} and 100 mA h g^{-1} at 1000 mA g^{-1} and 197.6 mA h g^{-1} upon reverting back to 100 mA g^{-1} after 110 cycles and a reversible long stable capacity of 160.8 mA h g^{-1} at 100 mA g^{-1} even after 2000 cycles (Fig. 5**b**). This electrochemical performance of V_4O_9 against Li is far superior compared to other reported vanadium oxide-based cathode hosts (Table S2) including those that are made composite with mesoporous/ high surface-area carbonaceous materials (like graphene, CNT etc). Premkumar *et al.*, cycled V_4O_9 against Li between 1.8 – 3.5 V at C/10 rate using carbonate based organic electrolyte and obtained 225 mA h g^{-1} for 50 cycles [19]. To check the versatility of this voltage range, we cycled between 1.8 – 3.5 V potential range using Solvionićs LiFSI:PYR14 FSI (2:3 mol ratio) electrolyte, our V_4O_9 could intercalate only ~3.9 Li^+ corresponding to discharge capacity of ~300 mA h g^{-1} and first cycle Coulombic efficiency of 75.5% (Fig. S3a). And upon subsequent testing its rate capability at different current densities (10 – 1000 mA g^{-1}) and long cycle stability, the V_4O_9 exhibited excellent reversibility having delivered 93.4 mA h g^{-1} even after 2000 cycles at 100 mA g^{-1} current density (Fig. S3b). Though these electrochemical performances are outstanding however are inferior compared to the specific capacity of 160.8 mA h g^{-1} for V_4O_9 obtained between potential range of 1.5–4.0 V (Fig. 5) as described above. As deduced from postmortem morphological analysis, the cycled V_4O_9 electrode keeps its integrity even after 700 cycles at 100 mA g^{-1} supporting its superior electrochemical performance (Fig. S4).

To understand the overwhelming electrochemical performance, we explored the electrochemical reaction kinetics of V_4O_9 against Li between 1.5 – 4.0 V using various electrochemical analytical techniques such as electrochemical impedance spectroscopy (EIS), cyclic voltammetry (CV) and galvanostatic-intermittent-titration-technique (GITT) to determine the Li^+-diffusivity (D_{Li}^+) in the quasi-steady-state-equilibrium state as shown in Fig. 6. The impedance of the freshly prepared cell is studied using the Nyquist plot obtained using impedance spectroscopy between 0.1 MHz – 10 mHz (Fig. 6**a**). It consisted of a depressed semicircle at high frequency followed by an inclined line extending to lower frequency. This is well fitted with an equivalent electrical circuit (shown in Fig. 6**a inset**) in which R_s is assigned to the solution/electrolyte resistance; R_{ct} to the resistance-to-charge-transfer and Q_{DL} to the capacitance of the electrical double layer corresponding to charge accumulation at the electrode/electrolyte interfacial layer. R_{INT} is assigned to the resistance of interfaces formed by reaction of the electrode with the electrolyte and Q_{INT} to their capacitances. Due to the close relaxation frequencies, unambiguous separation of R_{ct} and R_{INT} has not been possible. The Li//V_4O_9 cell exhibited R_s = 22.6 Ω and R_{ct} + R_{INT} = 93.4 Ω (Fig. 6**a**), respectively, in the high and intermediate frequency ranges. The low R_s and R_{ct} + R_{INT} values correspond to enhanced electronic conductivity of V_4O_9 cathode and hence, supports its improved rate performances. At much lower frequency the response has been assigned to Warburg element semi-infinite diffusion pattern (W_d). Nevertheless, the response deviates from the ideal 45° spike indicating that under the AC perturbation limited diffusion produces charge accumulation on the electrode surface [31,32].

Fig. 6**b** shows the CV plot obtained at 0.1 mV s-1 for 5 cycles. The first discharge consists of four reduction peaks at 2.69, 2.43, 2.29, 1.88 V and two broad oxidation peaks at 2.21, 2.71 V upon charging to 4 V while the reduction peaks disappeared in the subsequent cycles as only one broad peak is observed in the second reductive wave.

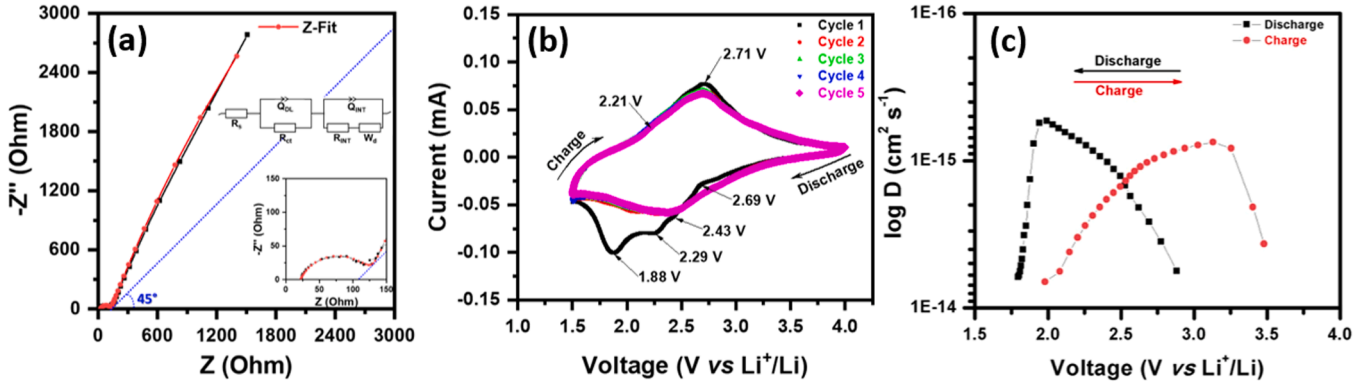

Fig. 6. (a) Experimental and fitted impedance spectra of a two-electrode cell at OCV (equivalent electrical circuit in the inset); (b) cyclic voltammogram scanned at 0.1 mV s^{-1}; (c) Li^+ chemical diffusion in V_4O_9 at various voltages in quasi-steady-state equilibrium state obtained using GITT method.

Interestingly, an excellent reversible behavior is observed after the first reduction of the V_4O_9 and hence, it anticipates superior electrochemical performances. Even though typical Faradic peaks developed in the first reduction disappear, the I-V profile with broad peaks embedded in a box-like profile points to the coexistence of both Faradic and capacitive charge storage mechanism. The former is expected to be limited at high current rate by Li^+-diffusivity.

To determine the Li^+-diffusivity, GITT is used. Before applying GITT, the cells were subjected to two discharge-charge cycles to avoid the capacity drop of the first cycle and achieve a steady state cycling. During GITT, we discharged-charged the cell by steps at 10 mA g^{-1} for 30 mins and relaxed in OCV for 8 h until their respective cut-off voltage (1.5 V for discharge and 4.0 V for charge) is reached whose plot is shown in Fig. S5. According to voltage-composition profile (see Fig. S5), the reaction with lithium proceeds through a solid solution, hence Li^+-diffusion process obeys Ficks law of diffusion. Upon simplification, the Li^+-diffusivity is given as [33,34]:

$$D_{Li^+} = \frac{4}{\pi}\left(\frac{IV}{FS}\right)^2 \left(\frac{\frac{dE}{dx}}{\frac{dE}{d\sqrt{t}}}\right)^2, t < L^2/D_{Li^+} \quad (1)$$

where D_{Li}^+ = chemical diffusion coefficient of the Li^+ ions ($cm^2\ s^{-1}$); V = molar volume ($cm^3\ mol^{-1}$) of the V_4O_9; F = Faraday's constant (96 485 C mol^{-1}), I = applied current (A), S = surface area of the active material in the electrode (cm^2) and L = diffusion length (cm). Using this equation, the logarithm diffusivity (log D) of Li^+ with respect to each voltage is plotted in the Fig. 6**c**. During discharge, the D_{Li}^+ decreases from 9.0×10^{-15} to 8.9×10^{-16} $cm^2\ s^{-1}$ corresponding nominally to ~3.8 Li^+ intercalation and then increases to 9.9×10^{-15} $cm^2\ s^{-1}$ and follows a reverse trend upon charging. The average D_{Li}^+ of V_4O_9 is 1.39×10^{-15} $cm^2\ s^{-1}$ corresponding to 2.53 V. This value is not as high as to allow for an excellent rate performance as expected for pure pseudo-capacitors and it explain that at very high current, V_4O_9 loses capacity as in a typical behaviour of a battery-like intercalation material. Nevertheless, it keeps an outstanding capacity of 160.8 mA h g^{-1} even after 2000 cycles. Thus, capacitive contribution has been investigated.

For this, we scanned CVs of V_4O_9 for 3 cycles at each scan rates varied between 1.5 – 0.01 mV s^{-1} as shown in Fig. S6. The area under CV graphs (Fig. S6) increases with scan rates represent the excellent electrochemical activity and charge-storage performance characteristics of V_4O_9 material.

To determine the charge/capacity contribution mechanism of V_4O_9, the CVs graphs at different scan rates (v) were used. The total area under the CV at each scan rate corresponds to the sum of diffusion-controlled (Faradic) and surface-controlled (pseudocapacitive or capacitive) charge storage mechanisms. These contributions could be determined using a power law wherein the peak current (i) and scan rate (v) are related by [35]:

$$i = a \times v^b \quad (2)$$

$$\log i = b \log v + \log a \quad (3)$$

where a and b are the variable parameters. The value b is obtained from slope of $log\ i$ vs $log\ v$ plot. If slope $b = 0.5$ then the Li^+ storage mechanism is Faradic, this is electron transfer, and hence charge storage, corresponds to intercalation/de-intercalation process. On the other hand, if slope $b = 1$ then charge is stored either in the electrical-double-layer (EDL) (capacitive) or in the surface associated to a redox process (pseudocapacitive) [36,37]. Therefore, the measured current (i) at each voltage (V) is the summation of these two storage mechanisms given as:

$$i = a_1 v + a_2 \sqrt{v} \quad (4)$$

where $a_1 \times v$ and $a_2 \times \sqrt{v}$ corresponds to capacitive and Faradic diffusion-controlled contributions, respectively wherein the constants, a_1 and a_2 are the slope and intercept from $I/\sqrt{v}$ against $\sqrt{v}$ plot. Fig. 7**a** and S7 shows the capacitive (red-color shaded region) and Faradic contribution towards total charge storage mechanism. The latter is related to diffusion of Li^+ by redox/Faradic reactions while red-colored region is non-diffusion that occurs at the particle surface which is capacitive or pseudocapacitive in nature. At low scan rate, say, at $v = 0.01\ mV\ s^{-1}$, the total charge storage mechanism is Faradic diffusion control with 62% while non-diffusion capacitance mechanism increases predominately to 83% (at $v = 1.5\ mV\ s^{-1}$) upon increasing the rates as shown in Fig. 7**b**. This is in accordance with the slope b against voltage plot (Fig. 7**c**) wherein the slope b at each potential is much greater than 0.5 which corresponds to capacitive or pseudocapacitive behavior. Thus, it has been demonstrated that although its voltage composition profile points to a capacitive behavior, V_4O_9 behaves also as an intercalation material. Due to low Li^+-diffusivity (1.39×10^{-15} $cm^2\ s^{-1}$), at high rate, Li^+ migration is not fast enough and capacity decreases at high current rate. Interestingly the capacity developed through the surface-controlled charge storage mechanism is high enough to consider V_4O_9 a promising cathode material whether the mechanism is surface redox pseudocapacitive or capacitive remains unknown, however the I-V voltage profile points to the former.

4. Conclusions

We successfully prepared least explored meta-stable 3D tunnel-type structured V_4O_9 nanoparticles using acetonitrile and nanoparticulate V_2O_5 as starting materials by novel solvothermal method. The as-prepared sample consisted of 5–20 nm average size V_4O_9 nanoparticles exhibiting mixed valence state (V^{4+}/V^{5+}) and an average oxidation state of 4.65 vanadium ions as deduced from XPS. Therefore, V_4O_9 showed an enhanced electronic conductivity which is reflected in their electrochemical performances. Upon discharge to 1.5 V, the V_4O_9 could intercalate ~6 Li^+ corresponding to 464.8 mA h g^{-1} at 10 mA g^{-1} and exhibited reversible 75.2% CE upon charging to 4.0 V. The V_4O_9 exhibited superior rate capability at various current densities for 110 cycles and excellent long cycle stability delivering a reversible capacity of 160.8 mA h g^{-1} at 100 mA g^{-1} even after 2000 cycles. The investigation of charge-storage mechanisms showed that the electrochemical performance of V_4O_9 is surface controlled at very high rate but can still be considered an intercalation material when used at lower or medium rate providing a total high capacity. Of special interest for V_4O_9 application is that it stands very long cycling making it a challenging/competitive cathode with high capacity and cyclability to replace expensive electrode compounds and to build a cost-effective plug-in electric vehicle.

CRediT authorship contribution statement

Guerrero-Pérez Olga: Validation. **M Subramaniyam Chandrasekar:** Conceptualization, Funding acquisition, Investigation, Methodology, Writing – original draft, Writing – review & editing. **García González Ester:** Data curation, Formal analysis. **Kuhn Alois:** Data curation, Formal analysis, Writing – review & editing. **García-Alvarado Flaviano:** Conceptualization, Funding acquisition, Supervision, Writing – review & editing. **Rodríguez-Castellón Enrique:** Formal analysis, Validation.

Declaration of Competing Interest

The authors declare that they have no known competing financial interests or personal relationships that could have appeared to influence the work reported in this paper.

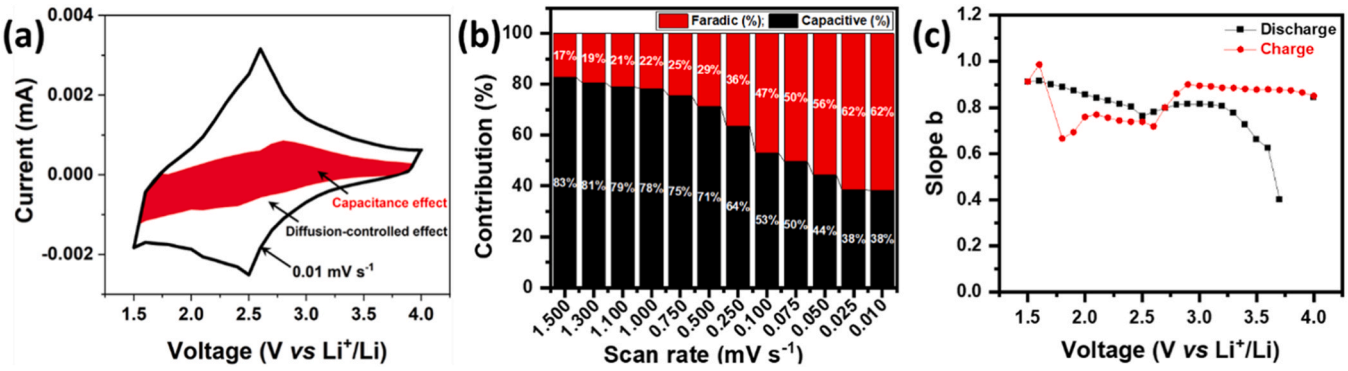

Fig. 7. (a) Mapping of the diffusion-controlled mechanism and capacitive effect in cyclic voltammogram at 0.01 mV s-1 rate; (b) Statistical contribution of Faradic and capacitive effect in V_4O_9 as a function of scan rates, ν (mV s^{-1}); (c) slope b (obtained from linear fit of *log i vs log* ν) as a function of each voltage during the discharge-charge process wherein concluding that the electrochemical kinetics of V_4O_9 to be dominated by the non-diffusive surface capacitive mechanism as the slope b values are >0.5.

Data availability

Data will be made available on request.

Acknowledgement

Chandrasekar M Subramaniyam acknowledges funding from the European Union's Horizon 2020 research and innovation programme under the Marie Skłodowska-Curie Actions (MSCA) grant agreement Number 898264. F.G, AK and E.G thank MCIN/AEI/10.13039/501100011033 for funding the projects PID2019-106662RB-C41, C44 and PID2022-139039OB-C21, C22. Financial support from the Universidad San Pablo is also acknowledged. Authors thank Centro Nacional de Microscopía Electrónica at Universidad Complutense de Madrid (ICTS ELECMI) for electron microscopy facilities and the SCAI of the University of Málaga for the BET experiments. O.G.P. and E.R.C. acknowledge project TED2021-130756B-C31 MCIN/AEI/10.13039/501100011033 and "ERDF A way of making Europe" by the European Union NextGenerationEU/PRTR.

Appendix A. Supporting information

Supplementary data associated with this article can be found in the online version at doi:10.1016/j.cattod.2024.114507.

References

[1] B. Dunn, H. Kamath, J.-M. Tarascon, Science 334 (2011) 928–935.
[2] M. Winter, R.J. Brodd, Chem. Rev. 104 (2004) 4245–4270.
[3] G.E. Blomgren, J. Electrochem. Soc. 164 (2017) A5019.
[4] K. Mizushima, P.C. Jones, P.J. Wiseman, J.B. Goodenough, Mater. Res. Bull. 15 (1980) 783–789.
[5] M.M. Thackeray, W.I.F. David, P.G. Bruce, J.B. Goodenough, Mater. Res. Bull. 18 (1983) 461–472.
[6] A.K. Padhi, K.S. Nanjundaswamy, J.B. Goodenough, J. Electrochem. Soc. 144 (1997) 1188.
[7] Y. Uebou, S. Okada, M. Egashira, J.-I. Yamaki, Solid State Ion. 148 (2002) 323–328.
[8] S.-i Nishimura, M. Nakamura, R. Natsui, A. Yamada, J. Am. Chem. Soc. 132 (2010) 13596–13597.
[9] B. Wang, Y. Han, X. Wang, N. Bahlawane, H. Pan, M. Yan, Y. Jiang, iScience 3 (2018) 110–133.
[10] D. Larcher, J.M. Tarascon, Nat. Chem. 7 (2015) 19–29.
[11] P. Liu, K. Zhu, Y. Gao, H. Luo, L. Lu, Adv. Energy Mater. 7 (2017) 1700547.
[12] M. Liu, B. Su, Y. Tang, X. Jiang, A. Yu, Adv. Energy Mater. 7 (2017) 1700885.
[13] Y. Yue, H. Liang, Adv. Energy Mater. 7 (2017) 1602545.
[14] X. Zhang, X. Sun, X. Li, X. Hu, S. Cai, C. Zheng, J. Energy Chem. 59 (2021) 343–363.
[15] J. Prado-Gonjal, B. Molero-Sánchez, D. Ávila-Brande, E. Morán, J.C. Pérez-Flores, A. Kuhn, F. García-Alvarado, J. Power Sources 232 (2013) 173–180.
[16] A. Kuhn, J.C. Pérez-Flores, J. Prado-Gonjal, E. Morán, M. Hoelzel, V. Díez-Gómez, I. Sobrados, J. Sanz, F. García-Alvarado, Chem. Mater. 34 (2022) 694–705.
[17] P. Hu, P. Hu, T.D. Vu, M. Li, S. Wang, Y. Ke, X. Zeng, L. Mai, Y. Long, Chem. Rev. 123 (2023) 4353–4415.
[18] S. Yamazaki, C. Li, K. Ohoyama, M. Nishi, M. Ichihara, H. Ueda, Y. Ueda, J. Solid State Chem. 183 (2010) 1496–1503.
[19] P. Senguttuvan, E. Lee, B. Key, C.S. Johnson, Front. Chem. 11 (2023).
[20] K. Kawashima, K. Kosuge, S. Kachi, Chem. Lett. 4 (1975) 1131–1136.
[21] H. Pang, Y. Dong, S.L. Ting, J. Lu, C.M. Li, D.-H. Kim, P. Chen, Nanoscale 5 (2013) 7790–7794.
[22] M.K. Chine, F. Sediri, N. Gharbi, Mater. Res. Bull. 47 (2012) 3422–3426.
[23] Q. Wang, T. Sun, S. Zheng, L. Li, T. Ma, J. Liang, Inorg. Chem. Front. 8 (2021) 4497–4506.
[24] A. Hammouche, A. Hammou, Electrochim. Acta 32 (1987) 1451–1452.
[25] M.O. Guerrero-Pérez, Catalysts (2018).
[26] J.F. Brazdil, R.G. Teller, W.A. Marritt, L.C. Glaeser, A.M. Ebner, J. Catal. 100 (1986) 516–519.
[27] R. Nilsson, T. Lindblad, A. Andersson, J. Catal. 148 (1994) 501–513.
[28] P. Shvets, O. Dikaya, K. Maksimova, A. Goikhman, J. Raman Spectrosc. 50 (2019) 1226–1244.
[29] C. Julien, G.A. Nazri, O. Bergström, Phys. Status Solidi (b) 201 (1997) 319–326.
[30] C. Szczuka, R.-A. Eichel, J. Granwehr, ACS Appl. Energy Mater. 5 (2022) 449–460.
[31] K. Adams, A.F. González, J. Mallows, T. Li, J.H.J. Thijssen, N. Robertson, J. Mater. Chem. A 7 (2019) 1638–1646.
[32] D.J. Kim, R. Ponraj, A.G. Kannan, H.-W. Lee, R. Fathi, R. Ruffo, C.M. Mari, D. K. Kim, J. Power Sources 244 (2013) 758–763.
[33] J.S. Horner, G. Whang, D.S. Ashby, I.V. Kolesnichenko, T.N. Lambert, B.S. Dunn, A. A. Talin, S.A. Roberts, ACS Appl. Energy Mater. 4 (2021) 11460–11469.
[34] C.M. Subramaniyam, Z. Tai, N. Mahmood, D. Zhang, H.K. Liu, J.B. Goodenough, S. X. Dou, J. Mater. Chem. A 5 (2017) 1925–1929.
[35] V. Augustyn, P. Simon, B. Dunn, Energy Environ. Sci. 7 (2014) 1597–1614.
[36] Y. Gogotsi, R.M. Penner, ACS Nano 12 (2018) 2081–2083.
[37] J. Wang, J. Polleux, J. Lim, B. Dunn, J. Phys. Chem. C. 111 (2007) 14925–14931.